Suggested plausible structures for Titan's haze analogs using tandem mass spectrometry

Julien Maillard, Isabelle Schmitz-Afonso, Thomas Gautier, Carlos Afonso, Nathalie Carrasco

To cite this version:

Julien Maillard, Isabelle Schmitz-Afonso, Thomas Gautier, Carlos Afonso, Nathalie Carrasco. Suggested plausible structures for Titan's haze analogs using tandem mass spectrometry. Icarus, 2021, 358 (April), pp.114181. 10.1016/j.icarus.2020.114181 . insu-02982671

HAL Id: insu-02982671
https://insu.hal.science/insu-02982671v1

Submitted on 18 Nov 2020

Suggested plausible structures for Titan's haze analogs using tandem mass spectrometry

Julien MAILLARD[1,2*], Isabelle SCHMITZ-AFONSO[2], Thomas GAUTIER[1], Carlos AFONSO[2] and Nathalie CARRASCO[1]

[1] LATMOS/IPSL, Université Versailles St Quentin, Sorbonne Université, CNRS, 11 blvd d'Alembert, F-78280 Guyancourt, France

[2] Normandie Univ, COBRA UMR 6014 et FR 3038 Univ Rouen; INSA Rouen; CNRS IRCOF, 1 Rue Tesnière, 76821 Mont-Saint-Aignan Cedex France

*Corresponding author:

Julien MAILLARD

Laboratoire COBRA, 1 Rue Lucien Tesnière, 76130 Mont-Saint-Aignan, France

+33 (0)2 35 52 29 19

julien.maillard@ens.uvsq.fr

Abstract

Understanding the formation and composition of the organic photochemical haze produced in Titan's upper atmosphere is an important milestone in prebiotic chemistry, for the early Earth climate and for the origin of life. However, retrieving knowledge about this organic fog is limited because of non-sample return possibilities. Chemical analyses from previous laboratory experiments allowed to obtain molecular information from analogues of this haze that were produced on Earth. In the current work, we push forward our comprehension of the structure composing this complex sample using tandem mass spectrometry. This type of analysis allows to recover structural information thanks to the observation of systematic fragmentation patterns. Strong differences are found between soluble and insoluble fractions of the aerosols and putative structures are proposed. Both highly aromatic structures as well as archipelago-like structures were observed in the insoluble fraction. The soluble fraction contains chemical structures with weaker bonds, composed of small aromatics cores linked together by short chains.

Keywords:

Titan, atmospheric chemistry, haze, Structural analyses, Icy world, Tandem mass spectrometry

Graphical Abstract

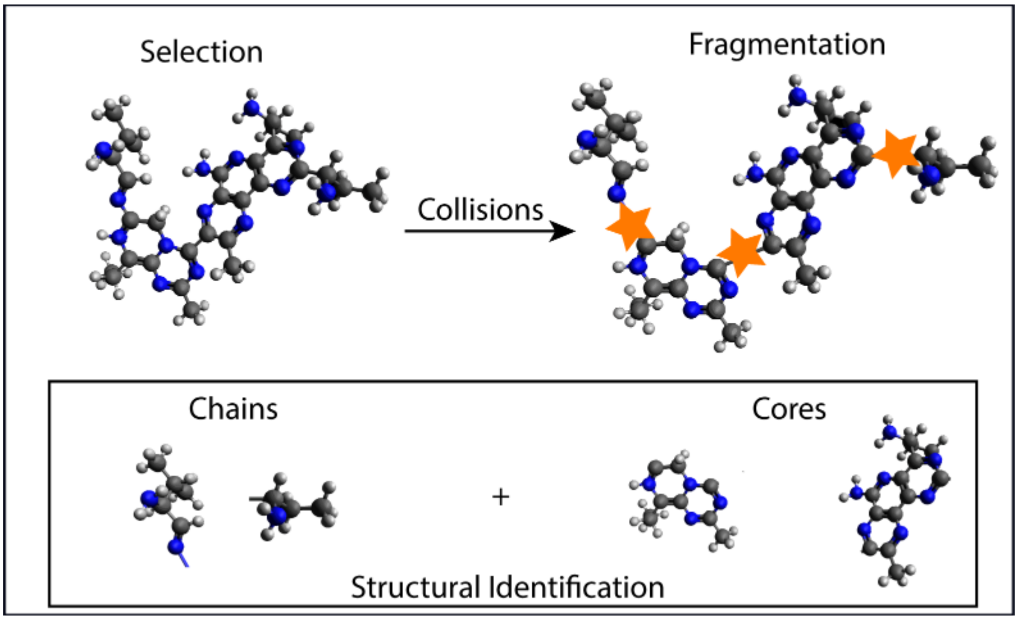

Introduction

Due to highly charged particles coming from Saturn's magnetosphere and UV photons from the sun, nitrogen and methane present in the upper atmosphere of Titan initiate an intense atmospheric chemistry chain (McKay et al., 1989; Sagan et al., 1993; Samuelson and A. Mayo, 1991). The very effective neutral and ion chemistry occurring induces the formation of large species than can be above 10 000 Da (Vuitton et al., 2009; Waite et al., 2007; Westlake et al., 2014) that end with the production of a complex organic haze lower in the atmosphere (Gupta et al., 1981; Sagan and Reid Thompson, 1984). This thick haze hides the surface of the largest satellite of Saturn (Israel et al., 2005). The Voyager and Cassini-Huygens space missions brought to light the importance of the carbon and nitrogen chemistry in the formation of this haze (Vuitton et al., 2006; Vuitton et al., 2019; Vuitton et al., 2007). However, due to the technical limitations of the onboard instruments, fully understanding the growing path of the haze particles is still out of range and many questions remain on their chemical composition. To address this issue, analogues of Titan's haze are produced on Earth (Coll et al., 1999; McKay et al., 1989; Poch et al., 2012; Sagan and Reid Thompson, 1984; Sciamma-O'Brien et al., 2010; Szopa et al., 2006; Trainer et al., 2006). These samples, called tholins, are analyzed in the laboratory with different analytical techniques. Several analyses, including infrared spectroscopy (Cable et al., 2014; Gautier et al., 2012; Imanaka et al., 2004), capillary electrophoresis (Cable et al., 2014) and nuclear magnetic resonance (Derenne et al., 2012; He and Smith, 2014b, 2015) revealed the presence of molecular families such as nitriles, amines and hydrocarbons. Few structures, regarding the complexity of the sample, such as triazine, pyrazole and pyrazine were identified thanks to liquid and gas chromatography coupled to ultrahigh resolution mass spectrometry (Gautier et al., 2014; Gautier et al., 2016). Mass spectrometry analyses revealed repetitive wave shapes in the mass spectra (Somogyi et al., 2005; Somogyi et al., 2012). A polymeric structure was suggested by several research teams (Matthews and Minard, 2006; Vuitton et al., 2010) . But even if a repetition unit of $(CH_2)_n$-$(HCN)_m$ was found to statistically explain the structure of tholins, the material is assumed to be not a pure polymer but rather a random one (Bonnet et al., 2013; Vuitton et al., 2010).

Recently, ultrahigh resolution mass spectrometry analyses through Fourier transform ion cyclotron resonance mass spectrometers have enabled an in-depth analysis of the chemical complexity of these tholins by generating global cartographies of the molecular diversity found in these samples (Maillard et al., 2018; Somogyi et al., 2012; Somogyi et al., 2016).

FTICR-MS is a state-of-the-art instrument, generally used to decipher the chemical composition of ultra-complex mixtures such as petroleum (Hughey et al., 2002; Le Maître et al., 2019; Marshall and Rodgers, 2008; Smith et al., 2018). This instrument allows an unprecedented resolving power and dynamic range (Nikolaev et al., 2011), making it ideal for the analysis of tholins samples which are an extremely complex material (Maillard et al., 2018). These analyses provide access to all the molecular formulae present in the sample. However, the isomeric and structural diversity remained unknown. In order to obtain an overview of the global structure present in tholins sample, ion mobility coupled with mass spectrometry was performed (Maillard et al., 2020; Ruger et al., 2019). These studies allowed for a narrowing of the possibilities of structures by excluding several families of compounds. Hypothetical structures obtained by theoretical calculations were also proposed.

Several tandem mass spectrometry analyses were previously performed in order to push the chemical characterisation (Somogyi et al., 2005; Somogyi et al., 2012) These studies have been performed on small species detected in the tholins sample (maximum *m/z* 190). They found systematic losses such as HCN and CH_2N_2 as well as evidence of aromatic structures. However, higher species were not studied. In this work, in order to get further evidence about the growth pathways and the structure of these tholins, tandem mass spectrometry (MS/MS) was performed at higher masses ($m/z > 400$).

Tholins samples studied here are from the PAMPRE experiment. They are mainly insoluble in methanol (Maillard et al., 2018). Using the combination of *electrospray* (ESI) and laser desorption ionization (LDI) coupled to a 12 T FTICR, results concerning the fragmentation of both fractions are reported in this work.

2. Methods

2.1. Analogues of Titan's aerosols production

Titan's aerosol analogues were produced with the PAMPRE experiment following the same procedure detailed in previous publications (Gautier et al., 2011; Szopa et al., 2006). The reactor is composed of a stainless-steel cylindrical reactor in which a RF-CCP discharge is established thanks to an RF 13.56 MHz frequency generator. A N_2:CH_4 95:5% gas mixture is injected in the chamber as a continuous flow through polarized electrodes and is then extracted by a primary vacuum pump to ensure that gases are homogeneously distributed. The plasma discharge is maintained at a pressure of 0.9 ± 0.1 mbar and at room temperature. A brown powder is recovered after few hours. Tholins are then stored in an inert atmosphere and protected from light. Limited oxidation occurs during the harvest, thus the oxygenated species are sorted out and are not studied during the mass spectrometry data treatment. It should be noted that the pressure and temperature are lower in Titan's ionosphere (respectively $\sim 10^{-5}$-10^{-8} mbar and 200 K) than in our experiment, but the ionization rate is the same (several CH4 molecules ionized over millions). As ion-molecule reaction rates are relatively insensitive to the temperature, the lower temperature in Titan's ionosphere (200K instead of 293K in the laboratory) is not an important issue in our case. The higher pressure ensures a faster kinetics in the experiment, and is low enough to limit termolecular reactions. The similar ionization rate enables a realistic contribution of ions into the whole ion-neutral coupled chemical network.

2.2. Sample preparation

To recover the soluble part of the sample, 4 mg of tholins are dissolved in 1 mL of methanol in a vial. The vial is vigorously stirred for 3 minutes to solubilize the maximum of species.

The brown mixture is then filtered using a 0.2 µm polytetrafluoroethylene (PTFE) membrane filter on a filter holder. The filtered solution is transferred into a vial and then analyzed after half dilution with a 50/50 water/methanol mixture. This sample preparation was made few minutes before the analysis in order to prevent the hydrolysis of the sample. The insoluble part is recovered for analysis.

2.3. Tandem mass spectrometry analysis

All analyses are performed on a hybrid quadrupole - FTICR Solarix XR from Bruker equipped with a 12 Tesla superconducting magnet and a dynamically harmonized ICR cell. The mass spectrometer is also equipped with an electrospray ionization source and a laser desorption ionization source (laser NdYAg×3 355 nm). The dynamically harmonized cell of the instrument was optimized using a design of experiments in order to obtain best spectra performance (Maillard et al., 2019). The mass spectrometer is externally calibrated with a solution of sodium trifluoroacetate. Afterwards, mass spectra are internally calibrated with confidently assigned signals. This calibration procedure yields to a mass accuracy below 300 ppb in the considered mass range. The following ion transfer parameters are used for both electrospray (ESI) and laser desorption ionization (LDI) analyses in positive ion mode: *m/z* 78 to 1200, capillary exit 150 V, deflector plate 200 V, funnel1 150 V, skimmer1 15 V, funnel RF amplitude 60 V_{pp}, octopole frequency 5 MHz, octopole RF amplitude 350 V_{pp}, lower cut-off of the quadrupole at *m/*z 93, time-of-flight 0.6 ms, frequency TOF 6 MHz, TOF RF amplitude 200 V_{pp}, side kick offset -1 V, front and back trapping plate 1.75 V. The soluble fraction was analyzed with *electrospray* ionization. Insoluble fraction is deposited using a solvent-free method, following a previously published procedure (Barrere et al., 2012) before being analyzed by laser desorption ionization. Both ionization methods were compared between themselves in a previous work (Maillard et al., 2018). The same molecules were detected for the soluble fraction by the two ionization sources. This suggests that in this study, it is valid to compare both the soluble and insoluble fractions even though the ionization mechanism is different.

Tandem mass spectrometry experiments are carried out using collision-induced dissociation (CID) in order to produce fragments (Chacon-Patino et al., 2017, 2018a, b; Rüger et al., 2017). This technique is based on the acceleration of mass selected ions species into a collision cell filled with a neutral gas such as argon or nitrogen, generating laboratory collisional energies. The extent of fragmentation generated depends on the nature of the target gas, the pressure and acceleration voltage applied (Shukla and Futrell, 2000). A scheme of the instrument is given in **figure S1** in order to have a better comprehension of experiments carried out here. To sum up, the first selecting quadrupole allowed for isolation of a defined *m/z* range which is then fragmented in the collision cell. Resulting fragments are detected in the ICR cell. Tandem mass spectrometry is performed using collision energy values ranging from 0 eV to 60 eV. This variation of acceleration voltages allows to induce more fragmentation and so, the apparition of new fragments. This process allows for a better understanding of the fragmentation pathway. For the nominal mass fragmentation, a window of one Dalton was set around the selected mass in order to isolate as few peaks as possible to simplify the comprehension of the analysis. Experiments were recorded in triplicates and only species recovered in the three triplicates were considered as real. Data treatment was carried out using DataAnalysis 5.0, OriginPro and Matlab. In addition, the collision energy in the laboratory frame of reference (E_{lab} in eV) is defined by $E_{lab}=z\times\Delta V$ with z as the charge of the ion. Because the detected ions are singly-charged, the collision energy applied to the precursor ions is equal to the used acceleration voltage

3. Results

In order the obtain the maximum information about tholins, several types of tandem experiments were conducted. Experiments without mass selection were evaluated for the insoluble and soluble species. In this experiment, the selecting quadrupole is not set as a filter but only as an ion guide, meaning that all ions generated are fragmented in the collision cell. However, regarding the lack of information given by these experiments due to the extremely high complexity of this sample, results of this broadband CID are only reported in supporting information by the **Figure S2** and **S3**. Nominal mass fragmentation was carried out on three nominal masses for the insoluble and soluble fraction. As the conclusions between each mass are the same, only the fragmentation of the nominal mass 504 will be discussed in the rest of this study. The two others masses (*m/z* 304 and *m/z* 404) are reported in supporting information by **figure S4 – S5**.

Figure 1 displays representative tandem mass spectra obtained from mass selected ions (*m/z* 504 nominal mass) for the insoluble and soluble fraction. The inset above each spectrum shows the same isolated species without acceleration voltages. Many species are co-isolated by the selecting quadrupole due to its low mass resolution (< 3000). Therefore, it is impossible to study particular/individual species, and all following results are reported using global views and molecular maps.

The first observation that is recovered from **Figure 1** is the strong difference in the fragment ion distribution between both fractions. In order to have a better understanding of what is happening, energy resolved mass spectra are given in **Figure 2** for each fraction showing the evolution of precursor ions relative intensity depending on the collision energy. As observed, when the fragmentation starts for the insoluble fraction around 20 eV, soluble precursors are already fragmented at 66%.

Even if the ionisation source is different between the soluble and the insoluble fraction, this highlights the fact that species present in the insoluble fraction are harder to break than in the soluble fraction. In our previous work, we have shown that the difference at the molecular level between each fraction is related to the number of unsaturations (Maillard et al., 2018). The insoluble fraction species present in average a higher number of unsaturations compared to the soluble fraction. With the insoluble fraction, at 40 eV collision energy, major fragment peaks are close to the precursor peak at *m/z* 504 indicating that they are produced through small neutral molecules losses. In contrast, major peaks in the soluble fraction are located under *m/z* 200 indicating that mainly relatively high mass neutral losses are produced. The insoluble fraction presents a relatively low H/C ratio which is consistent to more aromatic species that are more stable and are therefore harder to fragment. In addition, the loss between major peaks is different in both fractions. Several HCN are lost in the insoluble part whereas several NH_3 are lost in the soluble one. In order to go further in the description of both fractions, each one will be discussed separately in the rest of the manuscript.

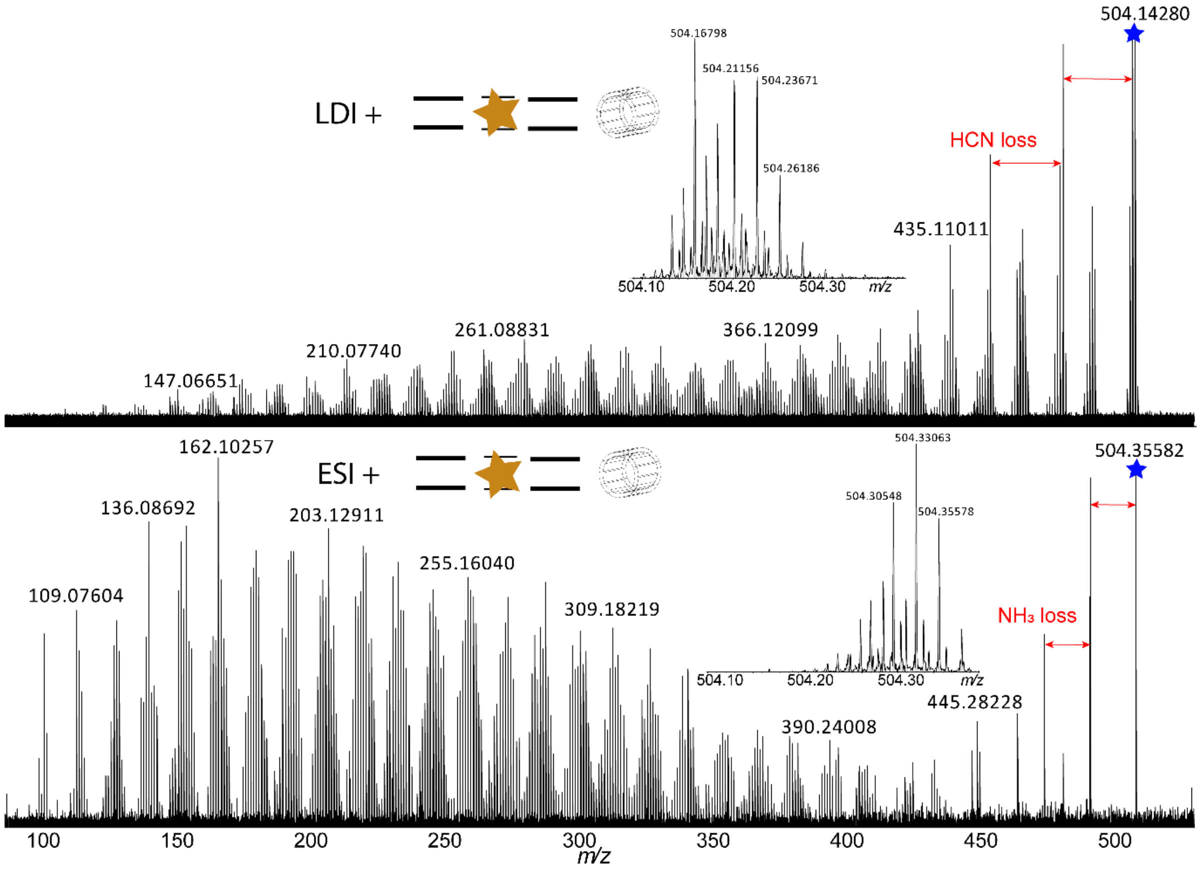

Figure 1: Fragmentation of the nominal mass 504 Da at 40 eV. (Top) Insoluble fraction, (Bottom) Soluble fraction.

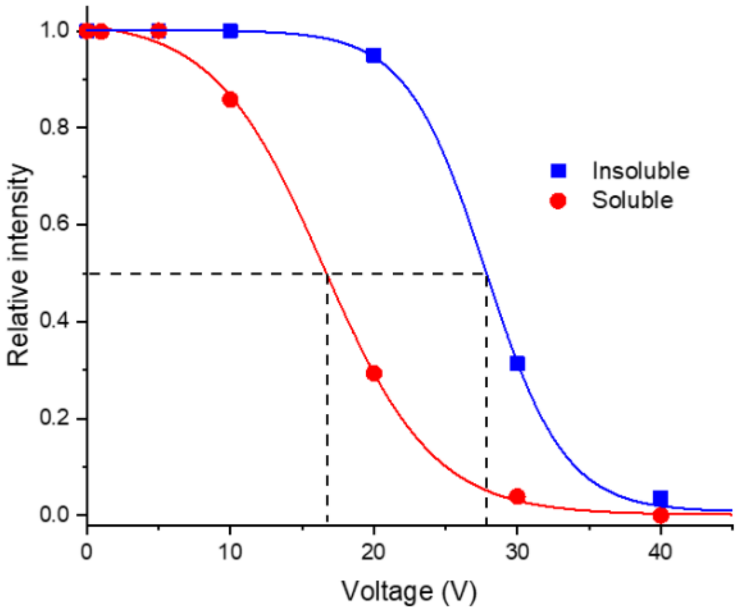

Figure 2: Energy resolved mass spectra of the insoluble (blue) and soluble (red) precursor species of the nominal mass 504.

3.1. Fragmentation of the species detected in the insoluble fraction

In this section, the fragmentation of species presents in the methanol insoluble fraction is studied. **Figure 3** displays the results obtained for one nominal mass (*m/*z 504) which was isolated monoisotopically and fragmented at different voltages. The Double Bond Equivalent (DBE) *vs* carbon number map is commonly used to visualize the diversity of compounds present in a complex sample or to observe particular fragmentation patterns(Chacon-Patino et al., 2017, 2018a, b; Le Maître et al., 2019). This metric is defined by equation 1 and represents the amount of unsaturation present in a molecule. In other words, the greater the DBE value, the more unsaturated the molecule.

(Equation 1)
$$DBE = C_{atoms} - \frac{H_{atoms}}{2} + \frac{N_{atoms}}{2} + 1$$

In addition, to highlight the degree of aromaticity of the fragment ions, polyaromatic hydrocarbon (planar limit) family has been added and is displayed by the red line (Cho et al., 2011). This family of compound is generally added to a DBE graph because it allows to compare the analysed sample with one of the most aromatic family containing only carbons and hydrogens atoms. This line is generated using benzene as starting point. The DBE and the number of carbons of successive linear additions of benzene to the initial point are then calculated. The resulting increase in DBE and number of carbons between two points is 3 and 4 respectively.

In **Figure 3**, each ion intensity is represented by the size of the circle and the amount of nitrogen contained in each species by a color code. **Figure 3a** plots the detected species present at *m/z* 504 with no collision energy. As mentioned before, many different ions at nominal masses *m/z* 504 are co-isolated due to the low resolution delivered by the quadrupole. Two main ions series appear at higher and lower DBE values. These series seem to have a similar number of carbons but a strong difference on the aromaticity degree. The more aromatic one will be called **series 1** and the other **series 2**. To illustrate this observation, putative structural formulas of compounds representative of the two major series were added in the Figure. These putative structures are based on hypotheses made in previous works(Gautier et al., 2017; Maillard et al., 2020; Ruger et al., 2019).

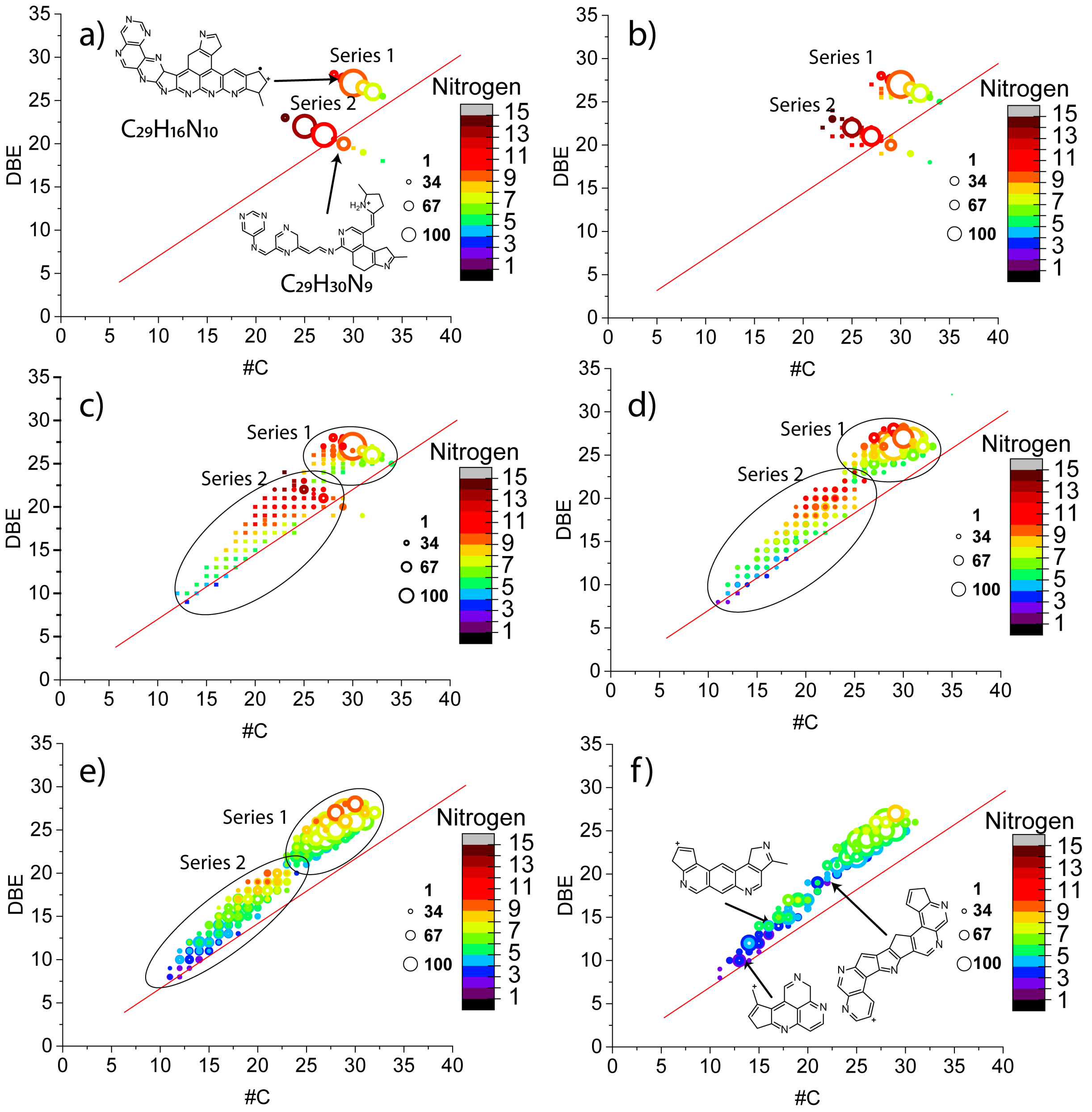

Figure 3: Nominal mass fragmentation of the *m/z* 504 insoluble displayed by DBE vs #C maps at a) 0 eV, b) 20 eV, c) 30 eV, d) 40e V, e) 50 eV and f) 60 eV collision energy, including some putative representative structures. The ions intensity is represented by the size of the circle and the amount of nitrogen contained in each species by the color code.

Two types of aromatic materials are observed by the **series 1** and **series 2**. The first series is much more aromatic than the other one and thus these two series are expected to have a different fragmentation pattern. **Figure 3b** reports the results for *m/z* 504 fragmented at 20 eV. Fragments for the two series are observed.

Less fragments are produced in the **series 1** in agreement with the fact that this series corresponds to more aromatic compounds and so, much more resistant to fragmentation. Due to the low resolution of the quadrupole used for mass selection, attributing fragments to one precursor is difficult regarding the number of isolated isobaric precursor ions. However, it can be observed that at 20 eV, the amount of DBE remains nearly constant for each series and mainly the amount of carbon is slightly decreasing (DBE value around 25 for the **series 1** and 20 for the **series 2**). This is consistent with a dealkylation process, meaning that peripheral alkyl branches are broken first.

Results at 30 eV are reported in **Figure 3c**. For the **series 2**, fragment ions presenting low DBE values compared to the precursor ions are observed. The N/C ratio which was at 0.330 for precursor species is measured for the fragments at a value of 0.325 which is roughly the same. In the case of tholins - unlike petroleum molecules - nitrogen atoms are likely being removed as neutral losses that would not counted as part of these DBE vs. C# diagrams (*vide infra*)(Le Maître et al., 2019). Indeed, the amount of nitrogen is responsible of a part of the DBE number as showed by the **equation 1**. However, exchanging a nitrogen atom for a carbon one will not alter the DBE value but will shift the amount of C. This is why we added the nitrogen amount as a color code. The **Figure 3c** color code reveals a decrease of the amount of nitrogen with the apparition of fragments at lower DBE. This observation highlights the loss of nitrogen atoms during the fragmentation. In addition, the **Figure S8** presents the corresponding van Krevelen diagrams showing the H/C vs N/C ratio in order to highlight the losses of nitrogen as well as the losses of DBE (through the increase of H/C ratio).

Figure 3d, 3e and 3f present the results obtained at 40 eV, 50 eV and 60 eV. The first observation is that no new fragments are observed in comparison with **Figure 3c** but there is mainly an increase of the intensity of previously detected species. This means that most easily breakable bonds were fragmented first.

Two types of aromatic materials can be considered from a previous study on asphaltenes fractions of petroleum(Chacon-Patino et al., 2018a): (*i*) small aromatic cores linked together by chains named *archipelago* or (*ii*) a large aromatic core with side chains named *island*. The rest of the section focuses on the obtained fragments in order to gain clues on the consistency the proposed models for the insoluble fraction of tholins.

For **series 1**, it can be observed that fragments remain around the precursor's region even at 40 eV and 50 eV. There is also no observation of nitrogen loss. At 60 eV, DBE, carbons and nitrogen losses starts to be observable. This means that the fragmentation of this series can be explained by three steps: In the first one, at low energy, peripheral bonds are broken, revealing in **Figure 3** a dealkylation pattern with some losses of DBE and nitrogen. Then, the fragmentation remains stable with an increasing energy until a certain level (between 50 eV and 60 eV). Finally, as observed in the **Figure 2f**, at high energies, large losses of DBE, carbons and nitrogen are observed, meaning that stronger bonds, such as aromatics rings are broken. This fragmentation process goes in favour of the island model for the **series 1**.

For **series 2**, the fragmentation process is slightly different from the other one and can be explained as follows. The first step of the fragmentation, at low energy, involves the rupture of weak bonds. As mentioned, during this step, large amount of DBE, carbons and nitrogen are lost. Then, no new fragments are observed during the increase of the collision energy.

Finally, such as for the **series 1,** between 50 eV and 60 eV, the fragmentation occurs again with losses of DBE, carbon and nitrogen. Large neutral losses during the first step go into favour of an *archipelago*-like model. Links between cores are broken and then at higher energy, ring opening occurs.

In conclusion, **Figure 4** presents two putative structures with the fragmentation scheme in agreement with all our observations for **series 1** and **series 2**.

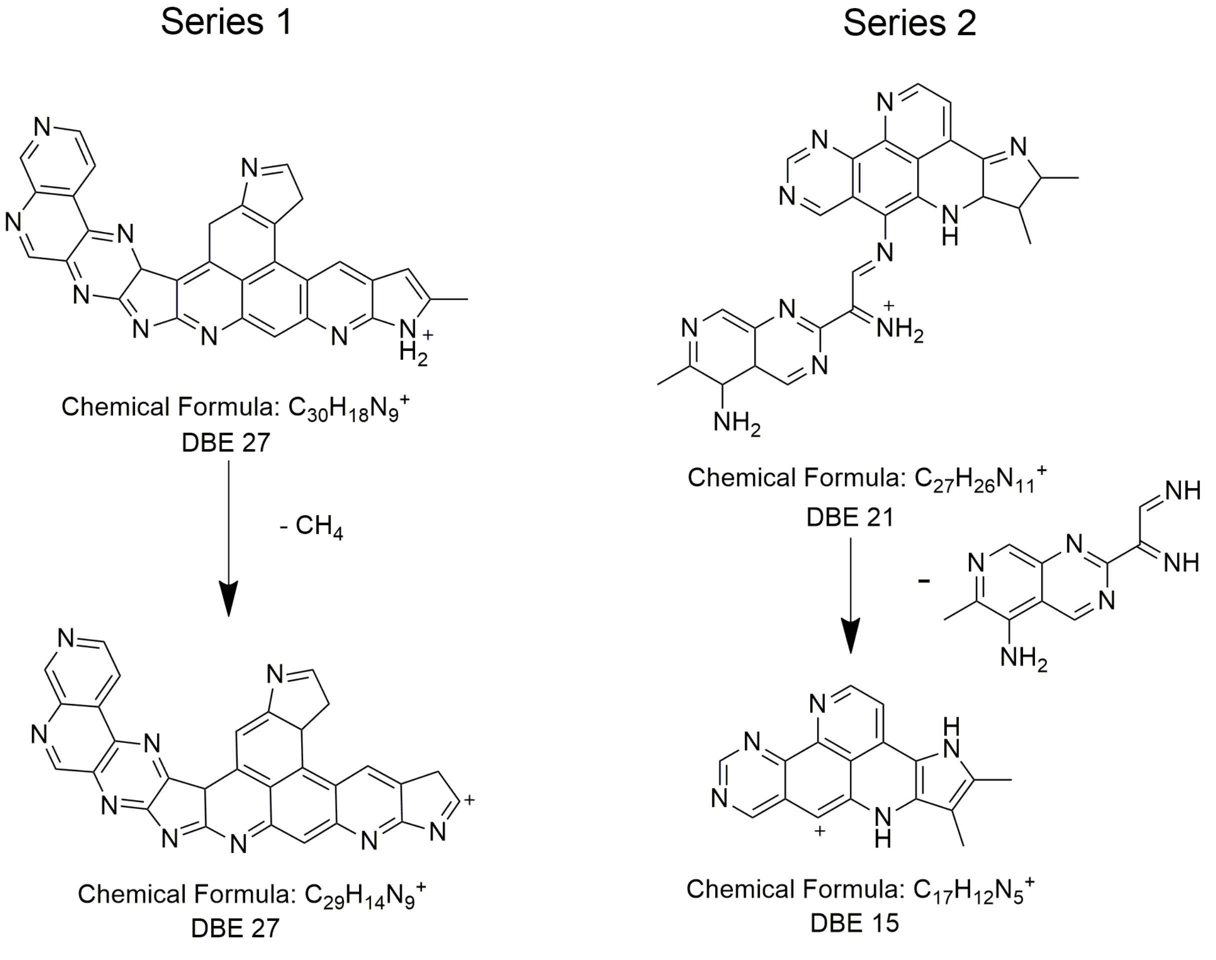

Figure 4: Hypothetical structures of one detected species at *m/z* 504 with (a) Archipelago type, (b) island type

3.2. Fragmentation of the species detected in the soluble fraction

In this part, as in the **section 3.1.**, the ions at *m/z* 504 were isolated and fragmented at different acceleration voltages in order to retrieve additional information about structures composing the soluble fraction. Results are illustrated by the **Figure 5**. In opposition with the insoluble fraction, only one series of compound is detected (**Figure 5a**); this series will be called **series 3**. As reported in previous work, the molecules of this fraction contain in average more hydrogen atoms than the insoluble fraction and present therefore a lower amount of unsaturations (Maillard et al., 2018). A hypothetical formula of one detected compound is described in **Figure 5a**.

At 5 eV (**Figure 5b)**, many fragments are already observed. Detected species are located lower and more on the left on the map, meaning that large losses of DBE and #C are observed. Such fragmentation at this low energy means that weak bonds are broken. Furthermore, the large losses of DBE reveal that the broken part of the precursor species contain DBE and aromatic rings because of the nonlinear intensities of the detected fragments (the most intense are highlighted by a red star).

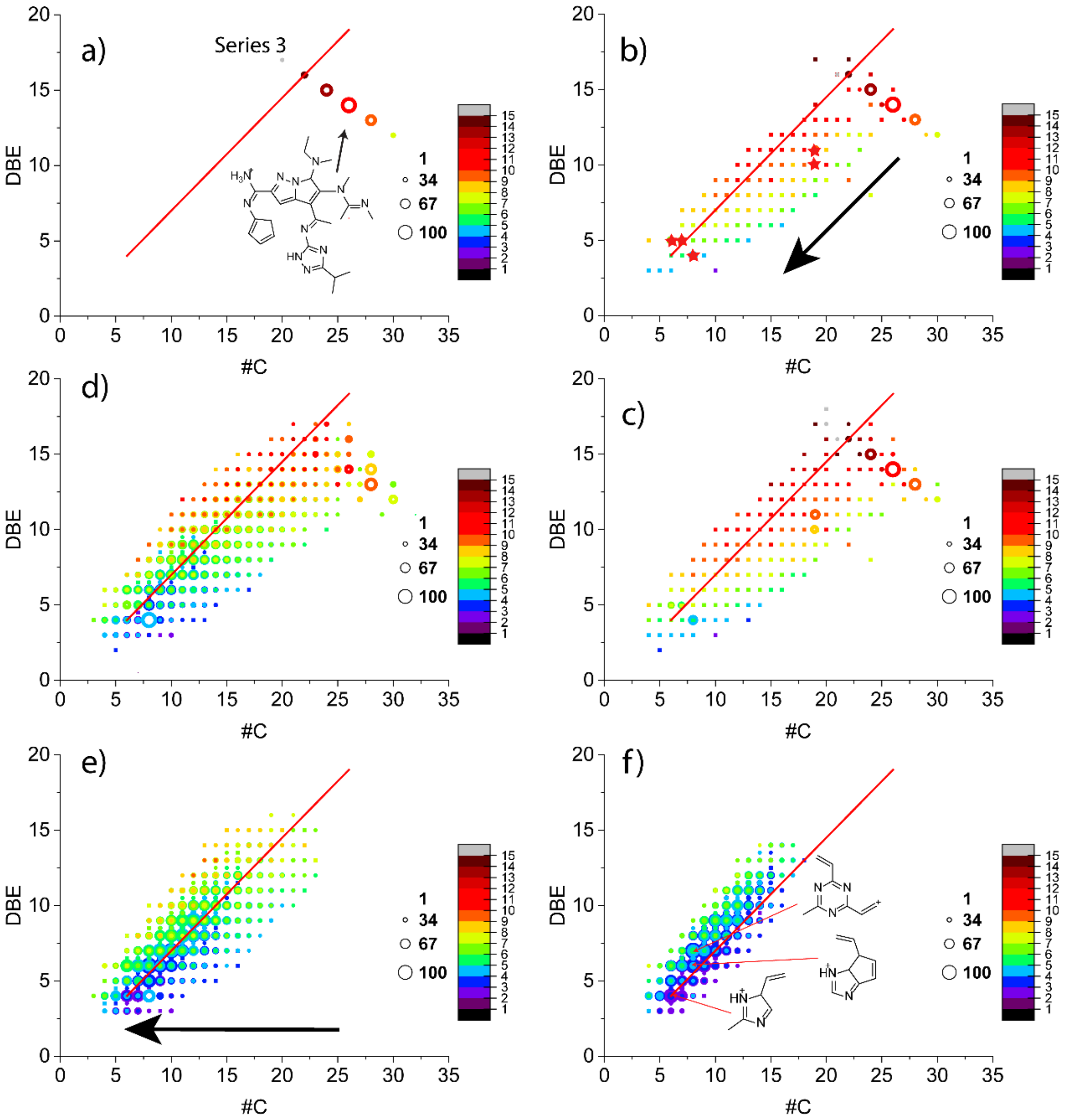

Figure 5 : Nominal mass fragmentation of the *m/z* 504 soluble fraction displayed by DBE vs #C maps at (a) 0 eV, (b) 5 eV, (c) 10 eV, (d) 30 eV, (e) 40 eV, (f) 60 eV collision energy, including some putative representative structures. The ions intensity is represented by the size of the circle and the amount of nitrogen contained in each species by the color code.

At other acceleration voltages, we observe no more losses of DBE. However, a dealkylation and denitrogenation is present as fragments are moving closer to the PAH line with the increase of the collision energy. **Figure S9** presents the corresponding van Krevelen diagrams showing the H/C vs N/C ratio in order to highlight the losses of nitrogen as well as the losses of DBE (through the increase of H/C ratio).

As for the insoluble species, this fragmentation can be explained in two distinct steps. First, at low energy, weak bonds between aromatic moieties are broken, showing large losses of DBE, carbon and nitrogen. Then, at higher energies, these moieties are dealkylated and denitrogenated. This fragmentation pattern is characteristic of an archipelago.

Regarding binding energies, the lower possible energy corresponds to the energy of a N – N binding, at 1.7 eV. The next one is the C – N binding with an energy of 3.192 eV. Imine bonds (C = N) have an energy of 7.856 eV: these kinds of bonds are not broken at this acceleration voltage. Thus, preferential encountered links between cores should be C – N bonds or N – N bonds in the soluble fraction. Several structures of the most intense detected species are given in the **Figure 5f**.

Finally, both models, islands and archipelagos, seem to be present in the sample, with islands more located in the insoluble fraction and archipelagos located in both fractions.

5. Conclusions and discussions

In this study, tandem mass spectrometry was performed on analogues of Titan’s haze. Due to the complexity of the analyzed sample, cartographies were used to facilitate the comprehension of the fragmentation patterns. Both insoluble and soluble fractions were studied. Fragmentation patterns were compared to island and archipelago models proposed in the literature. Island fragmentation was observed for the most aromatic family of the insoluble fraction. The second family was attributed to archipelagos because of the large losses of DBE observed at low collisional energies. Soluble structures were also attributed to archipelagos. On main difference between these two molecules is the higher aromaticity of the Figure 6b (DBE 19.5) vs the Figure 6c (13.5). The more aromatic molecules are, the more they tend to form aggregates and precipitate (Spiecker et al., 2003). As a summary, **Figure 6** shows three hypotheses of structures present in the tholins sample.

This work confirms structural hypotheses proposed in previous works performed by ion mobility concerning the presence of bulky structures in the soluble molecules (Maillard et al., 2020; Ruger et al., 2019). Such part of these structure were identified in several NMR studies (Derenne et al., 2012; He and Smith, 2014a, b) and liquid-chromatography-mass spectrometry analyses (Gautier et al., 2016). It has also allowed to go further into the chemical characterisation of the tholins by studying the major part, the insoluble fraction.

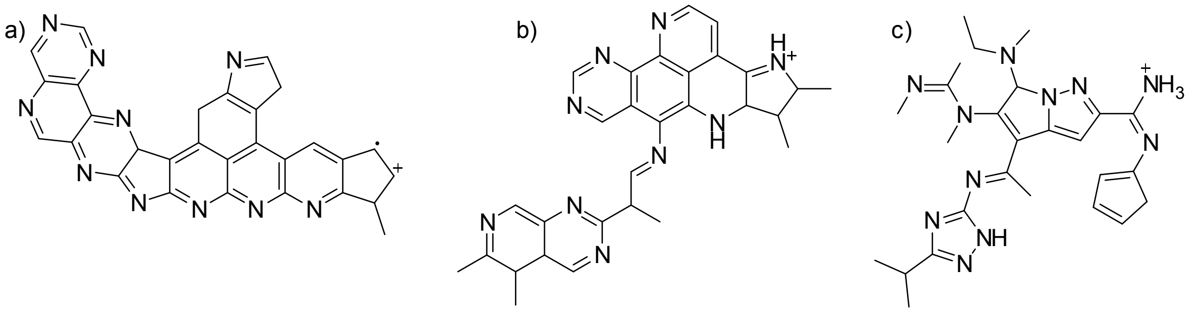

Chemical Formula: $C_{29}H_{16}N_{10}^{\bullet +}$
DBE = 27

Chemical Formula: $C_{29}H_{30}N_{9}^{+}$
DBE = 19.5

Chemical Formula: $C_{26}H_{38}N_{11}^{+}$
DBE = 13.5

Figure 6 : Hypotheses of structures for (a) Insoluble fraction **series 1**, (b) Insoluble fraction **series 2** and (c) Soluble fraction **series 3**

Retrieving such diversity of families for the compounds contained in Titan's tholins is an important information about Titan's haze. Firstly, such Nitrogenated-PAH structures are consistent with *in situ* measurements performed by the Cassini Huygens mission (Dinelli et al., 2013; López-Puertas et al., 2013). Then, regarding the recovered structures, soluble species are more fragile and much more reactive so they will react with their environment as a contrary to the insoluble ones which will deposit on the surface of the satellite.

Finally, in a previous work, tholins sample were analysed comparatively with FTICR and the LAB-Cosmorbitrap, an Orbitrap that is intended to be boarded in a space probe(Selliez et al., 2019). Large differences were observed between each analysis: higher masses were detected by FTICR compared to LAB-Cosmorbitrap, but the ions detected in the 100-200 u mass range were found the same. Fragmentation was very likely present with the cosmorbitrap analysis, induced by the difference of power delivered by the ionization laser. It is interesting to see that the fragmentation of such a complex mixture leads to new fragmented molecules consistent with the smaller non-fragmented molecules contained in the sample. And thus, studying these species is representative of larger masses. The use of a laser with tunable energy for the desorption/ionization source would be a promising technology to perform similar fragmentation experiments in space.

Acknowledgments

N.C. thanks the European Research Council for funding via the ERC PrimChem project (grant agreement No. 636829.).

This work was supported, at COBRA Laboratory, by the European Regional Development Fund (ERDF) N° HN0001343, the European Union's Horizon 2020 Research Infrastructures program (Grant Agreement 731077), the Région Normandie, and the Laboratoire d'Excellence (LabEx) SynOrg (ANR-11-LABX-0029). Access to a CNRS FTICR research infrastructure (FR3624) is gratefully acknowledged.

References

Barrere, C., Hubert-Roux, M., Lange, C.M., Rejaibi, M., Kebir, N., Desilles, N., Lecamp, L., Burel, F., Loutelier-Bourhis, C., 2012. Solvent-based and solvent-free characterization of low solubility and low molecular weight polyamides by mass spectrometry: a complementary approach. Rapid communications in mass spectrometry : RCM 26, 1347-1354.

Bonnet, J.-Y., Thissen, R., Frisari, M., Vuitton, V., Quirico, É., Orthous-Daunay, F.-R., Dutuit, O., Le Roy, L., Fray, N., Cottin, H., Hörst, S.M., Yelle, R.V., 2013. Compositional and structural investigation of HCN polymer through high resolution mass spectrometry. International Journal of Mass Spectrometry 354-355, 193-203.

Cable, M.L., Hörst, S.M., He, C., Stockton, A.M., Mora, M.F., Tolbert, M.A., Smith, M.A., Willis, P.A., 2014. Identification of primary amines in Titan tholins using microchip nonaqueous capillary electrophoresis. Earth and Planetary Science Letters 403, 99-107.

Chacon-Patino, M.L., Rowland, S.M., Rodgers, R.P., 2017. Advances in Asphaltene Petroleomics. Part 1: Asphaltenes Are Composed of Abundant Island and Archipelago Structural Motifs. Energy & Fuels 31, 13509-13518.

Chacon-Patino, M.L., Rowland, S.M., Rodgers, R.P., 2018a. Advances in Asphaltene Petroleomics. Part 2: Selective Separation Method That Reveals Fractions Enriched in Island and Archipelago Structural Motifs by Mass Spectrometry. Energy & Fuels 32, 314-328.

Chacon-Patino, M.L., Rowland, S.M., Rodgers, R.P., 2018b. Advances in Asphaltene Petroleomics. Part 3. Dominance of Island or Archipelago Structural Motif Is Sample Dependent. Energy & Fuels 32, 9106-9120.

Cho, Y., Kim, Y.H., Kim, S., 2011. Planar limit-assisted structural interpretation of saturates/aromatics/resins/asphaltenes fractionated crude oil compounds observed by Fourier transform ion cyclotron resonance mass spectrometry. Analytical chemistry 83, 6068-6073.

Coll, P., Coscia, D., Smith, N., Gazeau, M.-C., Ramirez, S.I., Cernogora, C., Israël, G., Raulin, F., 1999. Experimantal laboratory simulation of Titan's atmosphere: aerosols and gas phase. Planetary and Space Science 47, 1331-1340.

Derenne, S., Coelho, C., Anquetil, C., Szopa, C., Rahman, A.S., McMillan, P.F., Corà, F., Pickard, C.J., Quirico, E., Bonhomme, C., 2012. New insights into the structure and chemistry of Titan's tholins via 13C and 15N solid state nuclear magnetic resonance spectroscopy. Icarus 221, 844-853.

Dinelli, B.M., López-Puertas, M., Adriani, A., Moriconi, M.L., Funke, B., García-Comas, M., D'Aversa, E., 2013. An unidentified emission in Titan's upper atmosphere. Geophysical Research Letters 40, 1489-1493.

Gautier, T., Carrasco, N., Buch, A., Szopa, C., Sciamma-O'Brien, E., Cernogora, G., 2011. Nitrile gas chemistry in Titan's atmosphere. Icarus 213, 625-635.

Gautier, T., Carrasco, N., Mahjoub, A., Vinatier, S., Giuliani, A., Szopa, C., Anderson, C.M., Correia, J.-J., Dumas, P., Cernogora, G., 2012. Mid- and far-infrared absorption spectroscopy of Titan's aerosols analogues. Icarus 221, 320-327.

Gautier, T., Carrasco, N., Schmitz-Afonso, I., Touboul, D., Szopa, C., Buch, A., Pernot, P., 2014. Nitrogen incorporation in Titan's tholins inferred by high resolution orbitrap mass spectrometry and gas chromatography–mass spectrometry. Earth and Planetary Science Letters 404, 33-42.

Gautier, T., Schmitz-Afonso, I., Touboul, D., Szopa, C., Buch, A., Carrasco, N., 2016. Development of HPLC-Orbitrap method for identification of N-bearing molecules in complex organic material relevant to planetary environments. Icarus 275, 259-266.

Gautier, T., Sebree, J.A., Li, X., Pinnick, V.T., Grubisic, A., Loeffler, M.J., Getty, S.A., Trainer, M.G., Brinckerhoff, W.B., 2017. Influence of trace aromatics on the chemical growth mechanisms of Titan aerosol analogues. Planetary and Space Science 140, 27-34.

Gupta, S., Ochiai, E., Ponnamperuma, C., 1981. ORGANIC-SYNTHESIS IN THE ATMOSPHERE OF TITAN. Nature 293, 725-727.

He, C., Smith, M.A., 2014a. A comprehensive NMR structural study of Titan aerosol analogs: Implications for Titan’s atmospheric chemistry. Icarus 243, 31-38.

He, C., Smith, M.A., 2014b. Identification of nitrogenous organic species in Titan aerosols analogs: Implication for prebiotic chemistry on Titan and early Earth. Icarus 238, 86-92.

He, C., Smith, M.A., 2015. NMR study of the potential composition of Titanʹs lakes. Planetary and Space Science 109-110, 149-153.

Hughey, C.A., Rodgers, R.P., Marshall, A.G., 2002. Resolution of 11 000 Compositionally Distinct Components in a Single Electrospray Ionization Fourier Transform Ion Cyclotron Resonance Mass Spectrum of Crude Oil. Analytical chemistry 74.

Imanaka, H., Khare, B.N., Elsila, J.E., Bakes, E.L.O., McKay, C.P., Cruikshank, D.P., Sugita, S., Matsui, T., Zare, R.N., 2004. Laboratory experiments of Titan tholin formed in cold plasma at various pressures: implications for nitrogen-containing polycyclic aromatic compounds in Titan haze. Icarus 168, 344-366.

Israel, G., Szopa, C., Raulin, F., Cabane, M., Niemann, H.B., Atreya, S.K., Bauer, S.J., Brun, J.F., Chassefiere, E., Coll, P., Conde, E., Coscia, D., Hauchecorne, A., Millian, P., Nguyen, M.J., Owen, T., Riedler, W., Samuelson, R.E., Siguier, J.M., Steller, M., Sternberg, R., Vidal-Madjar, C., 2005. Complex organic matter in Titan's atmospheric aerosols from in situ pyrolysis and analysis. Nature 438, 796-799.

Le Maître, J., Hubert-Roux, M., Paupy, B., Marceau, S., Rüger, C., Afonso, C., Giusti, P., 2019. Structural analysis of heavy oil fractions after hydrodenitrogenation by high-resolution tandem mass spectrometry and ion mobility spectrometry. Faraday Discussions.

López-Puertas, M., Dinelli, B.M., Adriani, A., Funke, B., García-Comas, M., Moriconi, M.L., D’Aversa, E., Boersma, C., Allamandola, L.J., 2013. Large Abundances of Polycyclic Aromatic Hydrocarbons in Titan's Upper Atmosphere. The Astrophysical Journal 770, 132.

Maillard, J., Carrasco, N., Schmitz-Afonso, I., Gautier, T., Afonso, C., 2018. Comparison of soluble and insoluble organic matter in analogues of Titan's aerosols. Earth and Planetary Science Letters 495, 185-191.

Maillard, J., Ferey, J., Ruger, C.P., Schmitz-Afonso, I., Bekri, S., Gautier, T., Carrasco, N., Afonso, C., Tebani, A., 2019. Optimization of ion trajectories in a dynamically harmonized Fourier-Transform Ion Cyclotron Resonance cell using a Design of Experiments strategy. Rapid communications in mass spectrometry : RCM.

Maillard, J., Hupin, S., Carrasco, N., Schmitz-Afonso, I., Gautier, T., Afonso, C., 2020. Structural elucidation of soluble organic matter: Application to Titan's haze. Icarus, 113627.

Marshall, A.G., Rodgers, R.P., 2008. Petroleomics: chemistry of the underworld. Proceedings of the National Academy of Sciences of the United States of America 105, 18090-18095.

Matthews, C.N., Minard, R.D., 2006. Hydrogen cyanide polymers, comets and the origin of life. Faraday Discussions 133, 393.

McKay, C.P., Pollack, J.B., Courtin, R., 1989. The thermal structure of Titan's atmosphere. Icarus 80, 23-53.

Nikolaev, E.N., Boldin, I.A., Jertz, R., Baykut, G., 2011. Initial experimental characterization of a new ultra-high resolution FTICR cell with dynamic harmonization. Journal of the American Society for Mass Spectrometry 22, 1125-1133.

Poch, O., Coll, P., Buch, A., Ramírez, S.I., Raulin, F., 2012. Production yields of organics of astrobiological interest from H2O–NH3 hydrolysis of Titan's tholins. Planetary and Space Science 61, 114-123.

Ruger, C.P., Maillard, J., Le Maitre, J., Ridgeway, M., Thompson, C.J., Schmitz-Afonso, I., Gautier, T., Carrasco, N., Park, M.A., Giusti, P., Afonso, C., 2019. Structural Study of Analogues of Titan's Haze by Trapped Ion Mobility Coupled with a Fourier Transform Ion Cyclotron Mass Spectrometer. Journal of the American Society for Mass Spectrometry 30, 1169-1173.

Rüger, C.P., Neumann, A., Sklorz, M., Schwemer, T., Zimmermann, R., 2017. Thermal Analysis Coupled to Ultrahigh Resolution Mass Spectrometry with Collision Induced Dissociation for Complex Petroleum Samples: Heavy Oil Composition and Asphaltene Precipitation Effects. Energy & Fuels 31, 13144-13158.

Sagan, C., Khare, B.N., Thompson, W.R., McDonald, G.D., Wing, M.R., Bada, J.L., Vo-Dinh, T., Arakawa, E.T., 1993. Polycyclic aromatic hydrocarbons in the atmospheres of Titan and Jupiter. The Astrophysical Journal 414, 399.

Sagan, C., Reid Thompson, W., 1984. Production and condensation of organic gases in the atmosphere of Titan. Icarus 59, 133-161.

Samuelson, R.E., A. Mayo, L., 1991. Thermal infrared properties of Titan's stratospheric aerosol. Icarus 91, 207-219.

Sciamma-O'Brien, E., Carrasco, N., Szopa, C., Buch, A., Cernogora, G., 2010. Titan's atmosphere: An optimal gas mixture for aerosol production? Icarus 209, 704-714.

Selliez, L., Maillard, J., Cherville, B., Gautier, T., Thirkell, L., Gaubicher, B., Schmitz-Afonso, I., Afonso, C., Briois, C., Carrasco, N., 2019. High resolution mass spectrometry for future space missions: comparative analysis of complex organic matter with LAb-CosmOrbitrap and LDI-FTICR. Rapid communications in mass spectrometry : RCM.

Shukla, A.K., Futrell, J.H., 2000. Tandem mass spectrometry: dissociation of ions by collisional activation. Journal of Mass Spectrometry 35, 1069-1090.

Smith, D.F., Podgorski, D.C., Rodgers, R.P., Blakney, G.T., Hendrickson, C.L., 2018. 21 Tesla FT-ICR Mass Spectrometer for Ultrahigh-Resolution Analysis of Complex Organic Mixtures. Analytical chemistry 90, 2041-2047.

Somogyi, A., Oh, C.H., Smith, M.A., Lunine, J.I., 2005. Organic environments on Saturn's moon, Titan: simulating chemical reactions and analyzing products by FT-ICR and ion-trap mass spectrometry. Journal of the American Society for Mass Spectrometry 16, 850-859.

Somogyi, Á., Smith, M.A., Vuitton, V., Thissen, R., Komáromi, I., 2012. Chemical ionization in the atmosphere? A model study on negatively charged "exotic" ions generated from Titan's tholins by ultrahigh resolution MS and MS/MS. International Journal of Mass Spectrometry 316-318, 157-163.

Somogyi, A., Thissen, R., Orthous-Daunay, F.R., Vuitton, V., 2016. The Role of Ultrahigh Resolution Fourier Transform Mass Spectrometry (FT-MS) in Astrobiology-Related Research: Analysis of Meteorites and Tholins. International journal of molecular sciences 17, 439.

Spiecker, P.M., Gawrys, K.L., Kilpatrick, P.K., 2003. Aggregation and solubility behavior of asphaltenes and their subfractions. Journal of Colloid and Interface Science 267, 178-193.

Szopa, C., Cernogora, G., Boufendi, L., Correia, J.J., Coll, P., 2006. PAMPRE: A dusty plasma experiment for Titan's tholins production and study. Planetary and Space Science 54, 394-404.

Trainer, M.G., Pavlov, A.A., DeWitt, H.L., Jimenez, J.L., McKay, C.P., Toon, O.B., Tolbert, M.A., 2006. Organic haze on Titan and the early Earth. Proceedings of the National Academy of Sciences of the United States of America 103, 18035-18042.

Vuitton, V., Bonnet, J.-Y., Frisari, M., Thissen, R., Quirico, E., Dutuit, O., Schmitt, B., Le Roy, L., Fray, N., Cottin, H., Sciamma-O'Brien, E., Carrasco, N., Szopa, C., 2010. Very high resolution mass spectrometry of HCN polymers and tholins. Faraday Discussions 147, 495.

Vuitton, V., Lavvas, P., Yelle, R.V., Galand, M., Wellbrock, A., Lewis, G.R., Coates, A.J., Wahlund, J.E., 2009. Negative ion chemistry in Titan's upper atmosphere. Planetary and Space Science 57, 1558-1572.

Vuitton, V., Yelle, R.V., Anicich, V.G., 2006. The nitrogen chemistry of Titan's upper atmosphere revealed. Astrophys. J. 647, L175-L178.

Vuitton, V., Yelle, R.V., Klippenstein, S.J., Hörst, S.M., Lavvas, P., 2019. Simulating the density of organic species in the atmosphere of Titan with a coupled ion-neutral photochemical model. Icarus 324, 120-197.

Vuitton, V., Yelle, R.V., McEwan, M.J., 2007. Ion chemistry and N-containing molecules in Titan's upper atmosphere. Icarus 191, 722-742.

Waite, J.H., Jr., Young, D.T., Cravens, T.E., Coates, A.J., Crary, F.J., Magee, B., Westlake, J., 2007. The process of tholin formation in Titan's upper atmosphere. Science 316, 870-875.

Westlake, J.H., Waite, J.H., Carrasco, N., Richard, M., Cravens, T., 2014. The role of ion-molecule reactions in the growth of heavy ions in Titan's ionosphere. J. Geophys. Res-Space Phys. 119, 5951-5963.

Supporting Information

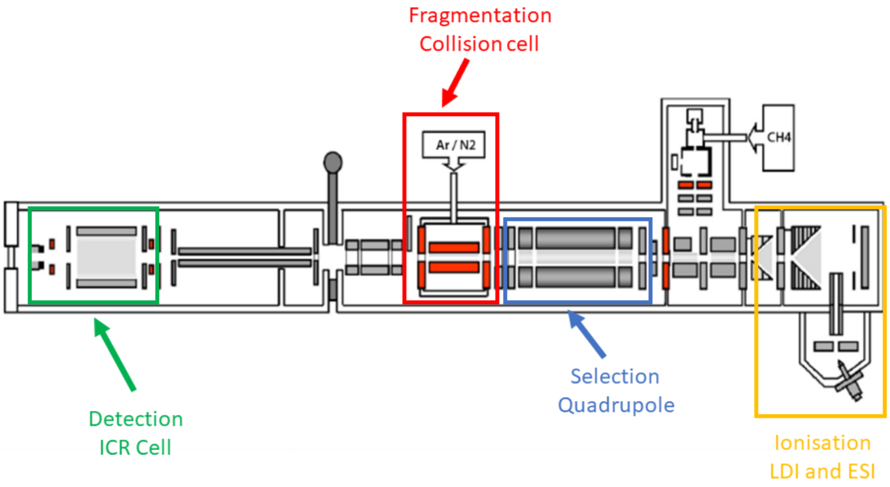

Figure S1: Schem of the instrument used for the tandem experiments

Figures S2a, S2b and S2c present the fragmentation obtained at respectively 0 eV, 10 eV and 20 eV using such visualization. At these collision energies, the cartographies look roughly similar except a shift in the DBE and number of carbons of the most intense species, those being represented with a red square on Figure 2. At 0 eV, the square is located between DBE 6 - 15 and #C 7 - 18. At 20 eV, the square is now located between DBE 5- 11, and #C 6 - 14. The area given by the square also becomes smaller as the energy increases. A loss of DBE and carbon is observed meaning that functional groups containing double bond are broken for voltages lower than 20 eV.

Figures S2d, S2e and S2f present the fragmentation of the insoluble fraction at 40 eV, 60 eV and 80 eV. At 40 eV, the global shape is thinner than at 20 eV. The species with DBE smaller than the aromatic red line are no more observable. The area of the red square continues to decrease, passing from DBE 5 – 12 and #C 6 – 14 at 30 eV to DBE 7 – 11 and #C 8 – 11 at 60 eV. At 80 eV, the same area as 60 eV is observed. By comparing the 0 eV and the 80 eV, a loss of DBE and #C is observed, passing from DBE 6 – 15 to DBE 7 – 11 and #C 7 – 18 to #C 8 – 11. We conclude that some fragmentation occurs, definitely with a loss of functions containing DBE and carbons. However, regarding these results, it is not excluded at this point that the loss of species is induced by the scattering in the collision cell. This phenomenon occurs at high acceleration energy when an ion collides with an atom of neutral gas and is deviated without being fragmented. It results in a loss of the ion without the formation of any fragment. In order to retrieve more information, nominal mass fragmentation is performed in the next section.

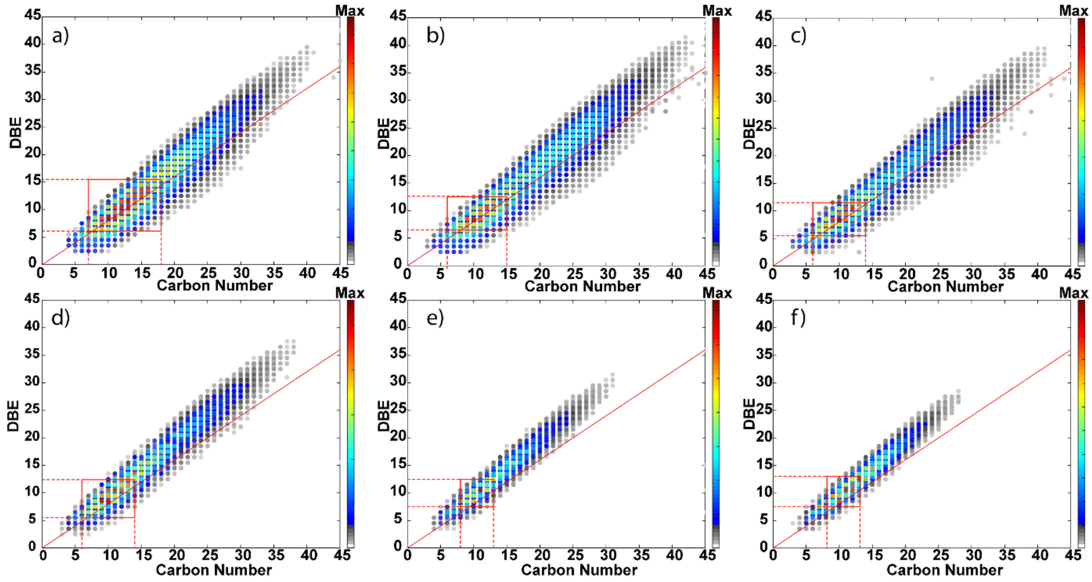

Figure S2: Broadband fragmentation of the Insoluble fraction displayed by DBE vs #C maps at a) 0 eV, b) 20 eV, c) 30 eV, d) 40 eV, e) 50 eV and f) 60 eV. The red line represent the PAH family and the red boxes highlights the most intense species detected in each mass spectra. Projection on each axes are also given in the figure.

This section targets the fragmentation of the second fraction recovered from the bulk tholins sample: the soluble fraction in methanol. At first, broadband CID has been performed on the sample and results are reported on **Figure S3**. By comparing the 0 eV maps and the results obtained for the 10 eV, we can see major peaks moving from DBE 3 – 11 to DBE 3 – 8 and the carbon number from 5 – 20 to 5 – 17. A loss of DBE and carbon is already observed even at this low energy. Between the 20 eV and the 60 eV energy, the value of DBE stays the same with a value between DBE 3 – 8. However, the #C decreases with the increase of the collision energy. Here, a large loss of DBE is observed at low energy in the first step. Then, the amount of carbons decreases with the increase of the collision energy. In order to go further on the understanding of this fragmentation, nominal mass CID was then performed.

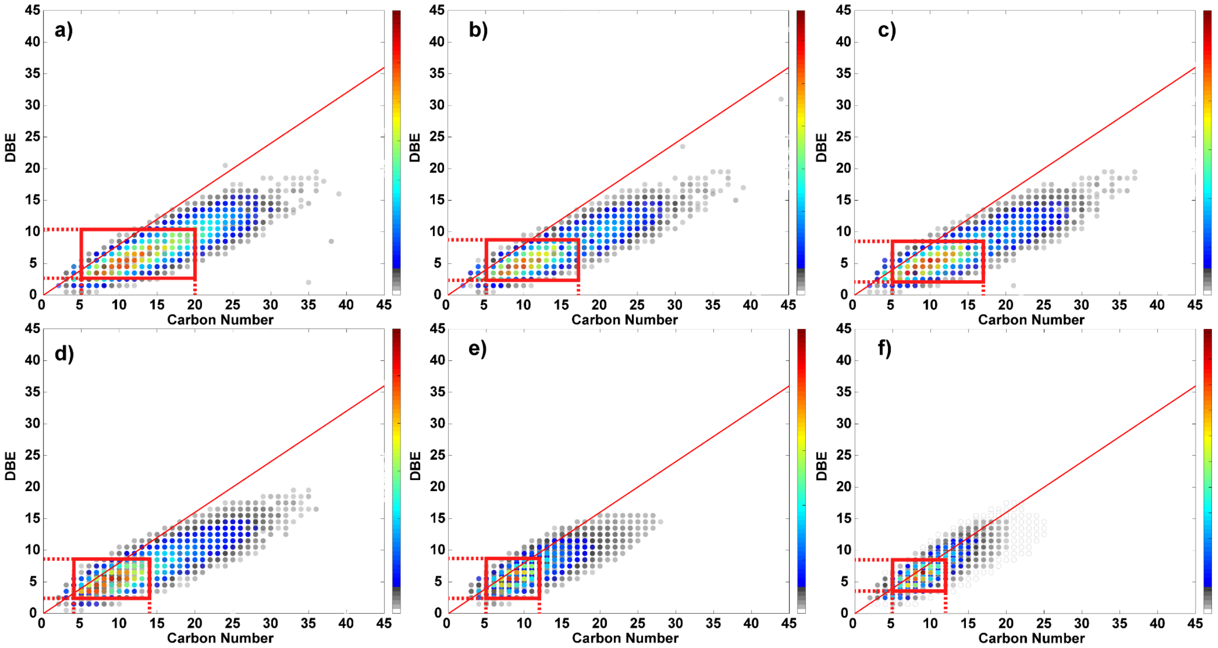

Figure S3 : Broadband fragmentation of the soluble fraction displayed by DBE vs #C maps at a) 0 eV, b) 10 eV, c) 20 eV, d) 30 eV, e) 40 eV and f) 60 eV. Species are color-coded by their intensities.

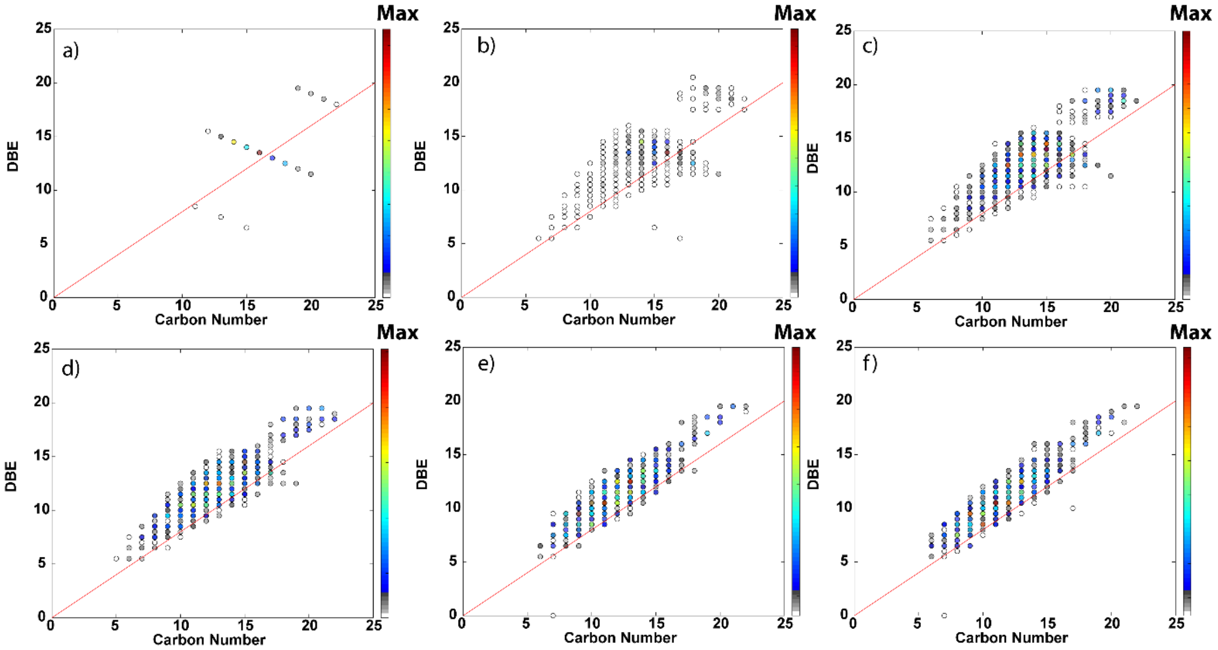

Figure S4: Nominal mass fragmentation of the *m/z* 304 insoluble displayed by DBE vs #C maps at a) 0 eV, b) 20 eV, c) 30 eV, d) 40 eV, e) 50 eV and f) 60 eV. Species are color-coded by their intensities.

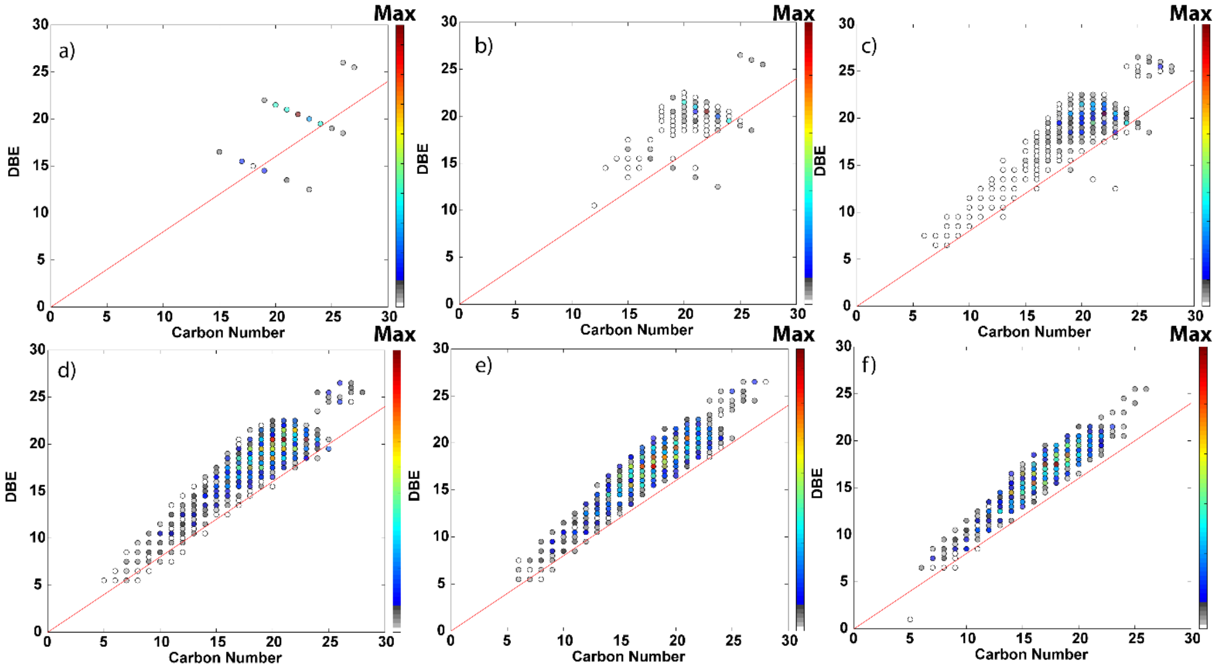

Figure S5: Nominal mass fragmentation of the *m/z* 404 insoluble displayed by DBE vs #C maps at a) 0 eV, b) 20 eV, c) 30 eV, d) 40 eV, e) 50 eV and f) 60 eV. Species are color-coded by their intensities.

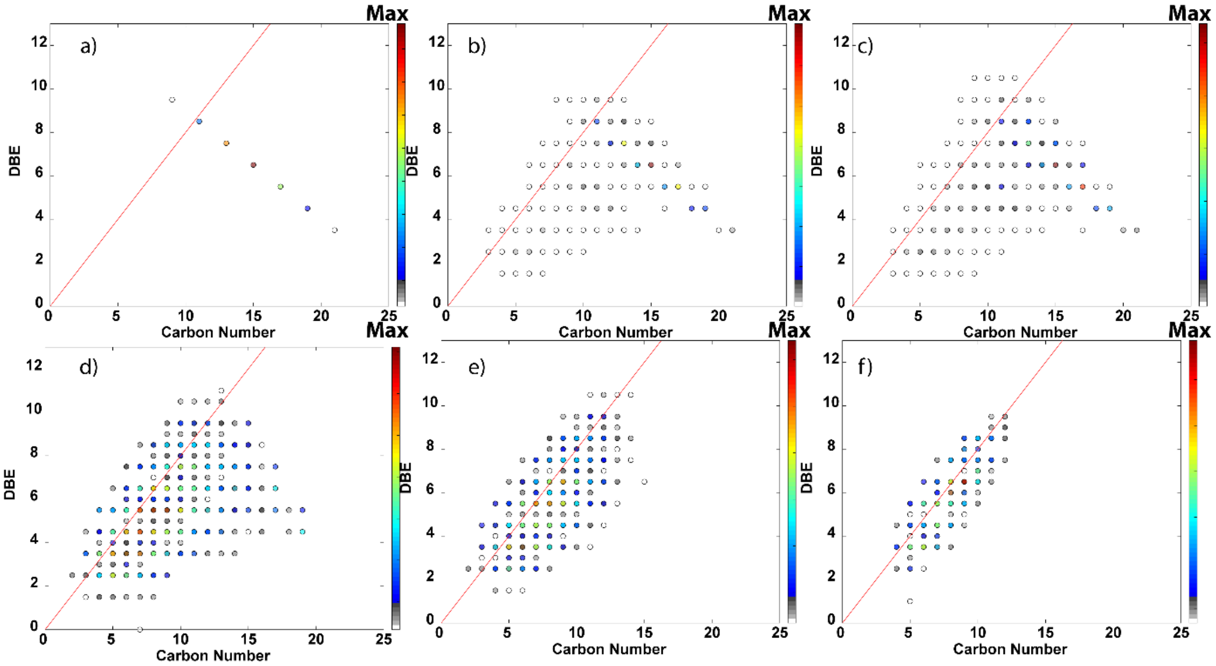

Figure S6: Nominal mass fragmentation of the *m/z* 304 Soluble displayed by DBE vs #C maps at (a) 0 eV, (b) 5 eV, (c) 10 eV, (d) 30 eV, (e) 40 eV, (f) 60 eV. Species are color-coded by their intensities.

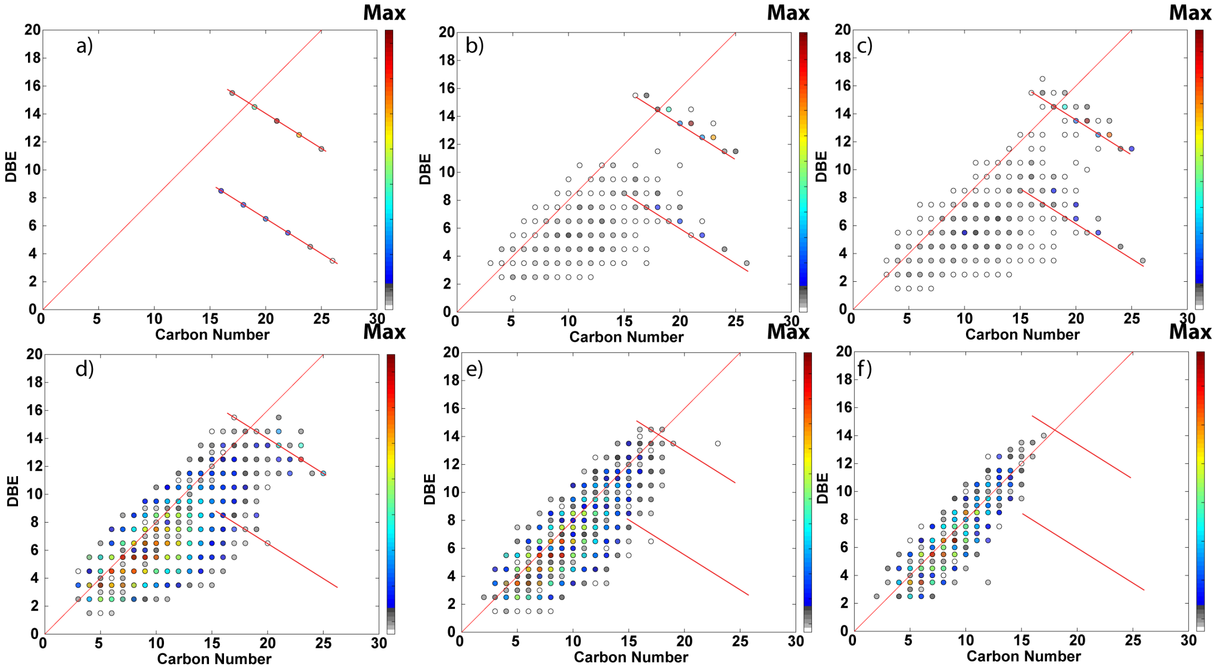

Figure S7: Nominal mass fragmentation of the *m/z* 404 soluble displayed by DBE vs #C maps at (a) 0 eV, (b) 5 eV, (c) 10 eV, (d) 30 eV, (e) 40 eV, (f) 60 eV. Species are color-coded by their intensities.

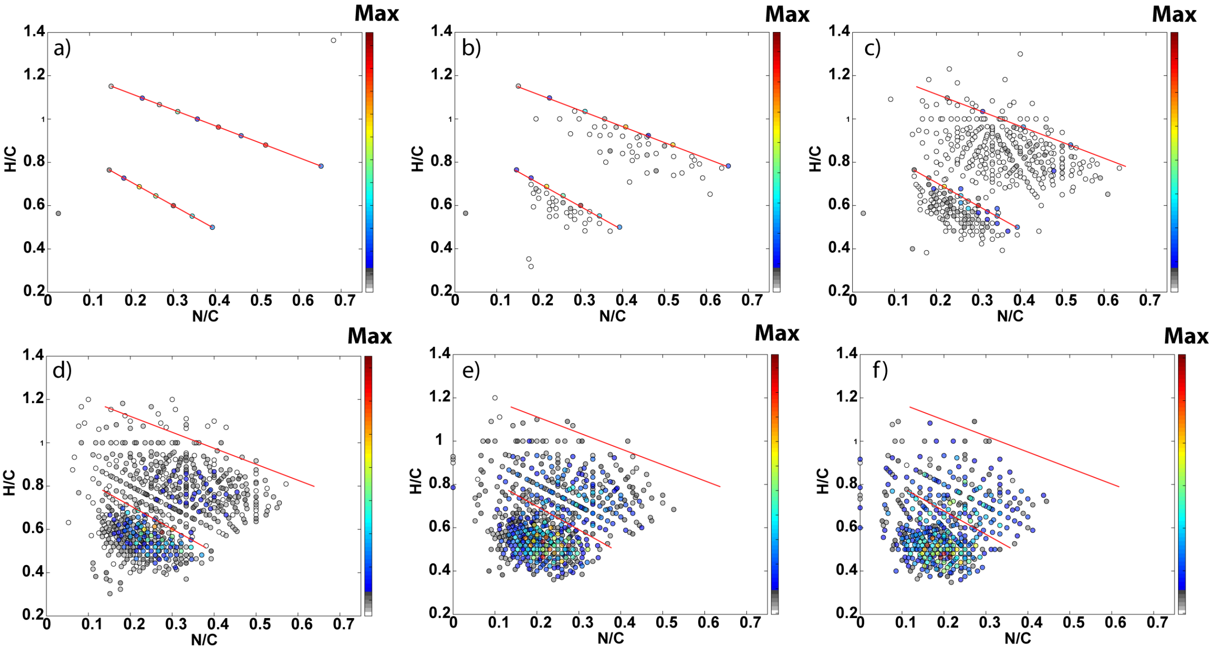

Figure S8: Van Krevelen diagrams obtained from the MS/MS spectra of *m/z* 504 insoluble recorded at a collision energy of a) 0 eV, b) 10 eV, c) 20 eV, d) 30 eV e) 40 eV, f) 60 eV. Species are color-coded by their intensities.

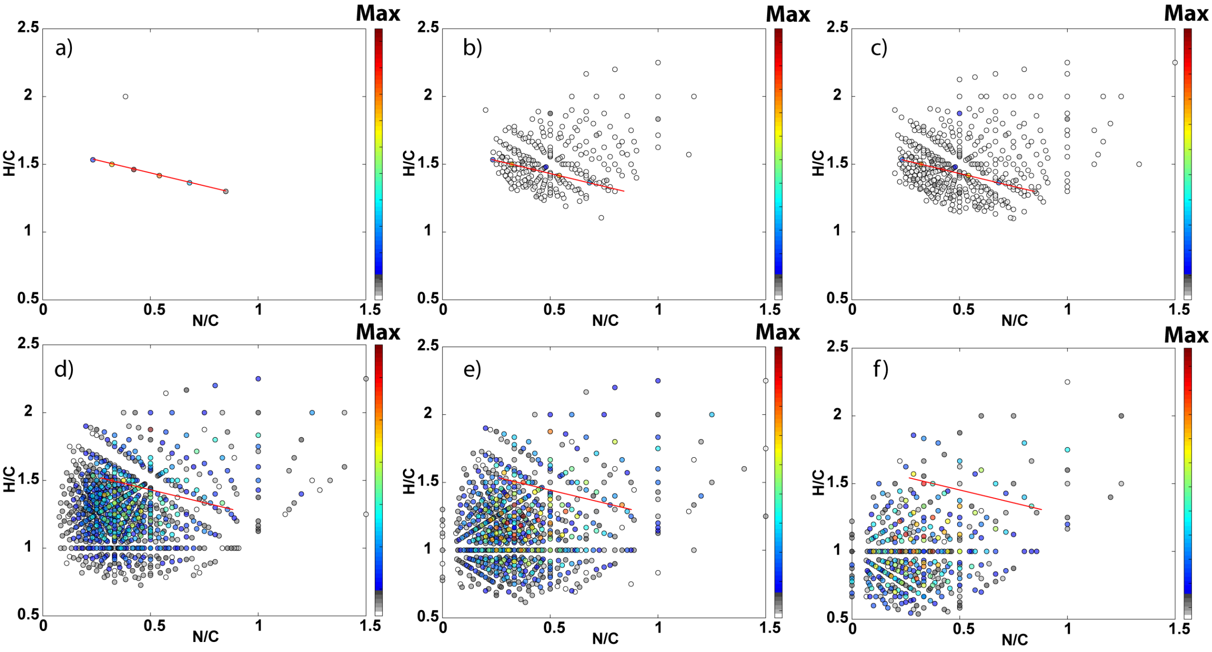

Figure S9: Van Krevelen diagrams obtained from the MS/MS spectra of *m/z* 504 soluble recorded at a collision energy of a) 0 eV, b) 5 eV, c) 10 eV, d) 30 eV e) 40 eV, f) 60 eV. Species are color-coded by their intensities.